Applied Thermal Engineering 165 (2020) 114576

Contents lists available at ScienceDirect

Applied Thermal Engineering

journal homepage: www.elsevier.com/locate/apthermeng

Research Paper

A comparative analysis of dynamic evaporator models for organic Rankine cycle waste heat recovery systems

Bin Xu[a], Dhruvang Rathod[a,*], Adamu Yebi[a], Simona Onori[b], Zoran Filipi[a], Mark Hoffman[c]

[a] Clemson University, Department of Automotive Engineering, 4 Research Dr., Greenville, SC 29607, USA
[b] Energy Resources Engineering Department, Stanford University, Stanford, CA 94305, USA
[c] Department of Mechanical Engineering, Auburn University, Auburn, AL 36849, USA

HIGHLIGHTS

- Identification of three evaporator models using the same experimental data.
- Comparison of modeling accuracy, computation cost, and modeling effort.
- Modeling selection suggestion based on the model comparison.
- 0-D lumped model is found to be accurate enough for many application purposes.

GRAPHICAL ABSTRACT

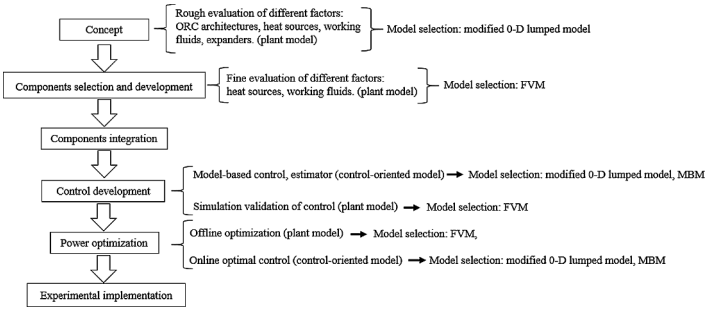

ARTICLE INFO

Keywords:
Waste heat recovery
Organic Rankine cycle
Model comparison
Heat exchanger model
Finite volume model
Moving boundary model

ABSTRACT

As the Organic Rankine Cycle Waste Heat Recovery (ORC-WHR) gained research attention in recent years, the evaporator models are required in plant modeling and model-based controls. However, model comparison and selection works are lacking in ORC-WHR application. Different from the modeling work in literature, this paper aims to first time present a comparative study of three evaporator models for Organic Rankine Cycle Waste Heat Recovery (ORC-WHR) systems using the same set of identification parameters and experimental data. Finite volume model and moving boundary model are the most popular modeling methodologies in the field of ORC-WHR. Meanwhile, 0-D lumped models attract some research attention thanks to their low computational cost and least modeling effort. This paper first presents the three models, which are then validated with experiments data collected in a heavy-duty diesel engine ORC-WHR system. In the model comparison process, accuracy, computational cost and modeling effort are evaluated. All three models exhibit decent working fluid vapor temperature prediction accuracy with 6.6 K of mean error and 1.27% mean error percentage both in steady state and transient conditions. 0-D lumped model is found to be accurate enough for many application purposes, which is not found in literature. Based on the comparison results, model selection recommendation is given based on disparate application purposes and different phases of ORC-WHR system development.

1. Introduction

As internal combustion (IC) engines continue to increase in efficiency, additional engine efficiency and emissions improvements come at an ever-increasing incremental cost. Meanwhile, IC engines still waste 30–60% of the fuel energy as heat through tailpipe (TP)

* Corresponding author.
E-mail address: dhruvar@clemson.edu (D. Rathod).

https://doi.org/10.1016/j.applthermaleng.2019.114576
Received 19 July 2019; Received in revised form 17 October 2019; Accepted 21 October 2019
Available online 21 October 2019

Nomenclature

A	area [m^2]
c_p	specific heat capacity [J/kg•K]
d	diameter [m]
h	enthalpy [J/kg]
k	thermal conductivity [W/m•K]
l, L	length [m]
m	mass [kg]/multiplier [-]
$\dot{m}$	mass flow rate [kg/s]
N	revolution speed [rpm]
Nu	Nusselt number [-]
O	valve opening [%]
p	pressure [Pa]
Re	Reynolds number [-]
t	time [s]
T	temperature [K]
u	velocity [m/s], internal energy [J/kg]
U	heat transfer coefficient [W/m^2•K]
v	dynamic viscosity [m^2/s]
V	volume [m^3]
x	vapor quality
z	space coordinate [m]
r	ratio
γ	specific heat ratio
ρ	density [kg/m^3]
∂	partial derivative operator
Pr	Prandtl number
ξ	friction factor

Abbreviations

0-D	0-dimensional
IC	internal combustion
ORC	organic Rankine cycle
WHR	waste heat recovery
TEG	thermoelectric generator
MBM	moving boundary method
FVM	finite volume method
EGR	exhaust gas recirculation
TP	tail pipe
PID	proportional-integral-derivative
EMC	electromagnetic compatibility
CAN	controller area network

Subscripts and superscripts

d	diameter
f	working fluid
w	tube wall separating working fluid and exhaust gas
g	exhaust gas
v	saturated vapor
l	saturated liquid
in	inlet/upstream
out	outlet/downstream
1, 2, 3	pure liquid, mixed, and pure vapor phase in MBM
p	pressure
	efficiency
U	heat transfer coefficient
TP	tail pipe
$tube$	heat exchanger tube
$shelleqv$	equivalent parameter in heat exchanger shell
$pure$	pure phase working fluid (either liquid or vapor)
mix	mix of liquid and vapor phase

exhaust gas, exhaust gas recirculation (EGR) cooler, charge air cooler, and engine coolant [1–3]. Thus far, waste heat recovery (WHR) technologies generating electricity or mechanical power have achieved 3–5% fuel economy improvement in experiments [1].

Popular WHR techniques include thermoelectric generator (TEG), turbocompounding, and organic Rankine cycle (ORC). TEG technique generates electricity from the temperature difference across the thermoelectric material [4,5]. It has the merits of lightweight and compact, while limited by the low efficiency and high cost of the thermoelectric materials [6]. Turbocompounding technique is generally considered in the heavy-duty diesel engine and installed after the turbocharger [7]. It extracts the engine waste energy and turns it into electricity [8] or mechanical power of crankshaft [9]. Like TEG, turbocompounding is compact. However, as the exhaust gas already undergoes an expansion process in the turbocharger, the efficiency of the second stage expansion in turbocompounding is not high. Among IC engine WHR technologies, the ORC has expediently gained traction thanks to its wide range of existing applications [10–12] and high recovery efficiency. Other than utilization of an organic working fluid, the ORC is fundamentally identical to the operational cycle of steam power plants. Steam power plants burn coal or oil to evaporate water and produce high pressure steam. Then the high pressure steam expands through a turbine, which rotates a generator for electricity production. Similarly, in the IC engine application, the ORC utilizes waste heat to evaporate the organic working fluid and produces high pressure vapor, which then passes through an expansion device to generate power. The schematic of the ORC system is shown in Fig. 1. The ORC-WHR researches in IC engine application have been soaring in the past decade. Both the academic institutes [13–15] and industry companies [1,16,17] get involved in the ORC-WHR techniques. The literature in this field can be grouped based on the different aspects as follows: modeling [18,19], control [20,21], optimization [15,22,23], component design [24,25], and experiments [1,26,27].

Accurate models are critical to all stages of ORC-WHR system development: design, simulation and optimization. Of all the ORC-WHR system components, heat exchanger modeling dominates the system physics and dynamics. The working fluid phase change occurring in the heat exchangers induces nonlinearities due to the disparate thermal properties of the liquid, vapor and mixed phases. Additionally, the evaporator determines the energy flow into the entire ORC system. Accurate energy source estimation is crucial for the accuracy of downstream parameters calculation. Therefore, the heat exchangers models play an important role in the ORC-WHR system modeling and are the focus of this work.

In current literature, three types of dynamic heat exchanger modeling methodologies permeate the ORC-WHR research landscape: (i) Finite volume method (FVM), (ii) Moving boundary method (MBM),

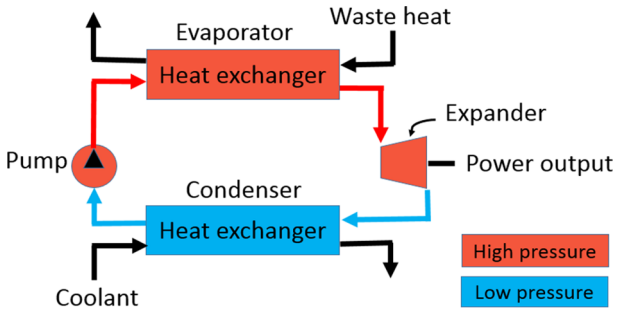

Fig. 1. Schematic of ORC in IC engine WHR application.

and (iii) 0-dimensional (0-D) lumped method. In the FVM, the heat exchanger is discretized into a number of uniform, fixed volume cells and the governing equations are solved in each cell. The MBM separates the heat exchanger into three cells based on the three working fluid phases (i.e. pure liquid phase, mixed phase and pure vapor phase). The volume of each cell freely varies during simulation and the two boundaries separating these three cells are tracked. Finally, a 0-D lumped modeling methodology does not utilize discretization, and is equivalent to the FVM when the number of discretization cells is set to unity.

The FVM has been widely utilized in the ORC-WHR offline heat exchanger plant modeling. Xu et al. implemented FVM for a tube-shell evaporator in a heavy-duty diesel engine ORC-WHR system and the model was validated with experimental data [18]. The same FVM model was used as the high fidelity plant model to evaluate three real-time implementable power optimization controls, which were Model Predictive Control, Machine Learning based real-time Dynamic Programming, rule-based proportional-integral-derivative (PID) control [15]. Quoilin et al. implemented FVM in a low-grade heat ORC-WHR application and the model was utilized as plant model to evaluate the different controls [23]. Grelet et al. used the FVM evaporator model to evaluate the fuel economy benefits of different working fluids and heat source configurations [28]. Additionally, Yousefzadeh et al. implemented the FVM in generalized ORC systems [29]. Lower order models are also derived from FVM to reduce the state number and computation cost, such as Proper Orthogonal Decomposition Galerkin Projection reduced model [30], and Hankel singular value model reduction [31].

The MBM is commonly utilized in ORC-WHR model-based control. Peralez et al. built a model-based feedforward control using the MBM in a heavy-duty diesel ORC-WHR application [32]. Combined with feedback PID control, the model-based feedforward control exhibited much less working fluid superheat tracking error than the standalone PID. Hou et al. constructed a model-based minimum variance control with MBM in a 100 kW ORC-WHR system attached to a power plant [33]. The results showed that the minimum variance control led to significant working fluid superheat variation reduction compared with PID control. Finally, BMW utilized the MBM in a passenger car ORC-WHR simulation and control design [34]. The model was identified and validated with experimental data.

0-D lumped model is generally utilized in the ORC-WHR concept development phase. Examples of such implementation are prevalent in literature. Battista et al. utilized a 0-D lumped model in a ORC-WHR limiting factors analysis in light duty vehicle applications [35]. The considered factors included engine back pressure, condenser sizing and weight, expander power output range, and vehicle frontal area. Chen et al. implemented a 0-D lumped model in a heavy-duty diesel ORC-WHR system [36]. The model was utilized to evaluate the heat exchanger volume and cost, expander power production range, ORC thermal efficiency, and engine efficiency improvement. Shu et al. analyzed potential working fluids with a 0-D lumped model in a diesel engine ORC-WHR system [37]. BMW utilized an experimentally validated 0-D lumped model to analyze the fuel consumption benefits of a BMW 5 Series with turbo-charged four-cylinder gasoline engine [2]. Peralez et al. implemented a 0-D lumped model in Dynamic Programming algorithm to optimizing ORC-WHR net power for its low state dimension and computational cost [38].

Even though the FVM, MBM and 0-D lumped modeling methods have been used frequently in the field of ORC-WHR, a systematic comparison of these three approaches is lacking in literature. Wei et al. [19] and Desideri et al. [39] compared the FVM and the MBM in the Modelica language. However, the parameter identification details were not specified. The authors are unware of any existing work comparing 0-D models with FVM and MBM for ORC-WHR applications. This paper simultaneously compares the FVM, MBM and 0-D lumped model. In addition, experimental data are rarely used in the heat exchanger modeling methods comparison for ORC-WHR application. In this work, the three models are identified and validated with experimental data at varying heat source conditions, which is collected from a heavy-duty diesel engine ORC-WHR system as reported in [18].

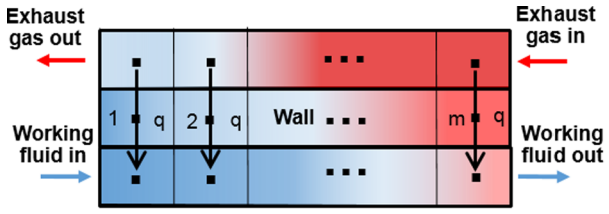

Fig. 2. Schematic of finite volume model with m cells discretization in a counter-flow scenario.

2. Modeling

The three modeling methods share the principles of mass and energy balance with adaptation to the specific modeling assumptions. The three evaporator models are built as Matlab m-script and run in the Matlab environment. Details of modeling work are given below.

2.1. The finite volume method

Under normal operating conditions, the working fluid comes into the heat exchanger as liquid, evaporates and exits as superheat vapor (moving from left to right in Fig. 2). Due to the fast exhaust gas mass flow dynamics, the exhaust gas mass flow rate is assumed to be identical across the heat exchanger. Heat conduction in the axial direction is neglected in all mediums (i.e. exhaust gas, wall, and working fluid). The momentum balance of the working fluid is not considered and pressure is assumed to be uniform across the heat exchanger for each flow. The governing equations of evaporator include working fluid mass balance, energy balance, wall energy balance, and exhaust gas energy balance, as presented in Eqs. (1), (2), (3) and (4) respectively.

Working fluid mass balance:

$$\frac{\partial(A_{f,cross}\rho_f)}{\partial t} + \frac{\partial \dot{m}_f}{\partial z} = 0 \tag{1}$$

Working fluid energy balance:

$$\rho_f A_{f,cross}\frac{\partial h_f(z,t)}{\partial t} = -\dot{m}_f\frac{\partial h_f}{\partial z} + \pi d_{tube}U_{f,w}(T_w - T_f) \tag{2}$$

Wall energy balance:

$$\rho_w C_{p,w}A_{w,cross}L\frac{dT_w(z,t)}{dt} = -A_{fw}U_{fw}(T_w - T_f) - m_\eta A_{g,w}U_{g,w}(T_w - T_g) \tag{3}$$

Exhaust gas energy balance:

$$\rho_g C_{p,g}A_{g,cross}\frac{\partial T_g(z,t)}{\partial t} = \dot{m}_g C_{p,g}\frac{\partial T_g}{\partial z} + \pi d_{shelleqv}U_{g,w}(T_w - T_g) \tag{4}$$

where m_η is a heat exchanger efficiency multiplier which accounts for heat losses from the exhaust gas to the environment. m_η will be identified with experimental data.

The FVM discretizes the entire heat exchanger into m cells in each medium (i.e. exhaust gas, wall, and working fluid) as shown in Fig. 2. m is the number of cells and q is the heat transfer. In each cell, heat is transferred from exhaust gas to the wall, and from the wall to the working fluid. The governing equations are solved in each cell. After the spatial discretization, Eqs. (1), (2), (3) and (4) for a single cell can be derived as follows:

Working fluid mass balance:

$$\frac{dm_f}{dt} = \dot{m}_{f,in} - \dot{m}_{f,out} \tag{5}$$

Working fluid energy balance:

$$m_f \frac{dh_f}{dt} = \dot{m}_{f,in} h_{f,in} - \dot{m}_{f,out} h_{f,out} + A_{fw} U_{fw} (T_w - T_f) \tag{6}$$

Wall energy balance:

$$m_w C_{pw} \frac{dT_w}{dt} = -A_{fw} U_{fw} (T_w - T_f) - m_\eta A_{gw} U_{gw} (T_w - T_g) \tag{7}$$

Exhaust gas energy balance:

$$m_g C_{pg} \frac{dT_g}{dt} = \dot{m}_{g,in} C_{pg} T_{g,in} - \dot{m}_{g,out} C_{pg} T_{g,out} + A_{gw} U_{gw} (T_w - T_g) \tag{8}$$

Boundary conditions are applied as follows: the inlet conditions of the n^{th} cell are the outlet conditions of cell $n-1$. The inlet conditions of first cell are experimentally measured at the heat exchanger inlet.

2.2. The moving boundary method

The second heat exchanger modeling method is the moving boundary method. The main idea behind this method is to track the boundaries separating the different working fluid phases. In the evaporation process, there are three different phases: liquid, mixed (both liquid and vapor) and vapor. These three phases are separated by two boundaries. The MBM calculates the positions of those two boundaries, namely boundary 1 and boundary 2, as shown in Fig. 3.

Temporal exhaust gas dynamics are neglected due to their fast transient characteristics. This assumption reduces the state dimensions and computational cost of the MBM. Exhaust gas and working fluid mass flow rate are assumed to be uniform across the entire heat exchanger. Energy balance is applied to the working fluid and the wall in each phase, resulting in a model with six states (three states for the working fluid, and three states for the wall) [40].

The MBM assumes the existence of all three working fluid phases within the heat exchanger. A six-state MBM model can be derived phase by phase using Eqs. (2) and (3). In the liquid phase, the working fluid and wall energy balance equations are derived as follows:

$$\dot{m}_{f,l} = \dot{m}_{f,in} - A_{f,cross} \left(L_1 \frac{\partial \rho_{f,1}}{\partial h_f} \frac{dh_{f,1}}{dt} + (\rho_{f,1} - \rho_l) \frac{dL_1}{dt} \right) \tag{9}$$

$$A_{f,cross} \rho_{f,1} (h_{f,1} - h_{f,l}) \frac{dL_1}{dt} = -\frac{1}{2} A_{f,cross} L_1 \left[\rho_{f,1} + \frac{\partial \rho_{f,1}}{\partial h_f} (h_{f,1} - h_{f,l}) \right] \frac{dh_{f,in}}{dt} + \dot{m}_{f,in} (h_{f,in} - h_{f,l}) + \pi d_{tube} L_1 U_{fw,1} (T_{w,1} - T_{f,1}) \tag{10}$$

$$A_{w,cross} C_{pw} \rho_w L_1 \frac{dT_{w,1}}{dt} + A_{w,cross} C_{pw} \rho_w (T_{w,1} - T_{w,l}) \frac{dL_1}{dt} = \pi d_{tube} L_1 U_{fw,1} (T_{f,1} - T_{w,1}) + m_\eta \pi d_{shelleqv} L_1 U_{g,w} (T_{g,1} - T_{w,1}) \tag{11}$$

In the mixed phase, the working fluid and wall energy balance equations are derived as follows:

$$\dot{m}_{f,v} = \dot{m}_{f,l} - A_{f,cross} \left(L_2 \frac{\partial \rho_{f,2}}{\partial h_f} \frac{dh_{f,2}}{dt} + (\rho_{f,2} - \rho_{f,v}) \frac{dL_2}{dt} + (\rho_{f,l} - \rho_{f,v}) \frac{dL_1}{dt} \right) \tag{12}$$

$$A_{f,cross} [\rho_{f,1} (h_{f,l} - h_{f,v})] \frac{dL_1}{dt} + A_{f,cross} (1 - \bar{\gamma}) [\rho_{f,l} (h_{f,l} - h_{f,v})] \frac{dL_2}{dt} = -\frac{1}{2} A_{f,cross} L_1 \frac{\partial \rho_{f,1}}{\partial h_f} \frac{dh_{f,in}}{dt} (h_{fl} - h_{f,v}) + \dot{m}_{f,in} (h_{f,l} - h_{f,v}) + \pi d_{tube} L_2 U_{fw,2} (T_{w,2} - T_{f,2}) \tag{13}$$

$$A_{w,cross} C_{pw} \rho_w L_2 \frac{dT_{w,2}}{dt} + A_{w,cross} C_{pw} \rho_w (T_{w,l} - T_{w,v}) \frac{dL_1}{dt} + A_{w,cross} C_{pw} \rho_w (T_{w,2} - T_{w,v}) \frac{dL_2}{dt} = \pi d_{tube} L_2 U_{fw,1} (T_{f,w} - T_{w,2}) + m_\eta \pi d_{shelleqv} L_2 U_{g,w} (T_{g,2} - T_{w,2}) \tag{14}$$

In the vapor phase, the working fluid and wall energy balance equations are derived as follows:

$$\dot{m}_{f,out} = \dot{m}_{f,v} - A_{f,cross} \left(L_3 \frac{\partial \rho_{f,3}}{\partial h_f} \frac{dh_{f,3}}{dt} + (\rho_{f,v} - \rho_{f,3}) \frac{dL_1 + dL_2}{dt} \right) \tag{15}$$

$$A_{f,cross} [\rho_{f,3} (h_{f,out} - h_{f,3}) + \rho_{f,1} (h_{f,v} - h_{f,out})] \frac{dL_1}{dt} + A_{f,cross} [\rho_{f,3} (h_{f,out} - h_{f,3}) + ((1 - \bar{\gamma}) \rho_{f,l} + \bar{\gamma} \rho_{f,v}) (h_{f,v} - h_{f,out})] \frac{dL_2}{dt} + \frac{1}{2} A_{f,cross} L_3 \left[\rho_{f,3} - \frac{\partial \rho_{f,3}}{\partial h_f} (h_{f,out} - h_{f,3}) \right] \frac{dh_{f,out}}{dt} = -\frac{1}{2} A_{f,cross} L_1 \left[\frac{\partial \rho_{f,1}}{\partial h_f} (h_{f,v} - h_{f,out}) \right] \frac{dh_{f,in}}{dt} + \dot{m}_{f,in} (h_{f,v} - h_{f,out}) + \pi d_{tube} L_3 U_{fw,3} (T_{w,3} - T_{f,3}) \tag{16}$$

$$A_{w,cross} C_{pw} \rho_w L_3 \frac{\partial T_{w,3}}{\partial t} + A_{w,cross} C_{pw} \rho_w (T_{w,v} - T_{w,3}) \frac{dL_1}{dt} + A_{w,cross} C_{pw} \rho_w (T_{w,v} - T_{w,3}) \frac{dL_2}{dt} = \pi d_{tube} L_3 U_{fw,3} (T_{f,3} - T_{w,3}) + m_\eta \pi d_{shelleqv} L_3 U_{g,w} (T_{g,3} - T_{w,3}) \tag{17}$$

where $L_3 = L - (L_1 + L_2)$, L is the total length of the evaporator. The exhaust gas temperature in each working fluid phase is derived from the right side of Eq. (4), as follows:

$$T_{g,1} = \frac{[\pi d_{tube} L_1 U_{g,w} T_{w,1} + \dot{m}_g C_{pg} \{2T_{g,2} - 2T_{g,3} + T_{g,in}\}]}{\dot{m}_g C_{pg} + \pi d_{tube} L_1 U_{g,w}} \tag{18}$$

$$T_{g,2} = \frac{[\pi d_{tube} L_2 U_{g,w} T_{w,2} + \dot{m}_g C_{pg} \{2T_{g,3} - T_{g,in}\}]}{\dot{m}_g C_{pg} + \pi d_{tube} L_2 U_{g,w}} \tag{19}$$

$$T_{g,3} = \frac{[\pi d_{tube} L_3 U_{g,w} T_{w,3} + \dot{m}_g C_{pg} T_{g,in}]}{\dot{m}_g C_{pg} + \pi d_{tube} L_3 U_{g,w}} \tag{20}$$

2.3. The 0-D lumped method

The third heat exchanger modeling method is the 0-D lumped method [38,41]. This method considers only a single, uniform volume for the working fluid, wall and exhaust gas, respectively as shown in Fig. 4. The 0-D lumped method schematic is similar to the FVM without the cell discretization. Ignoring the exhaust gas dynamics in the axial direction, the 0-D lumped model has two states corresponding to the working fluid and wall temperatures. The governing equations of 0-D lumped model is the same as the finite volume model as expressed in Eqs. (5), (6), (7) and (8).

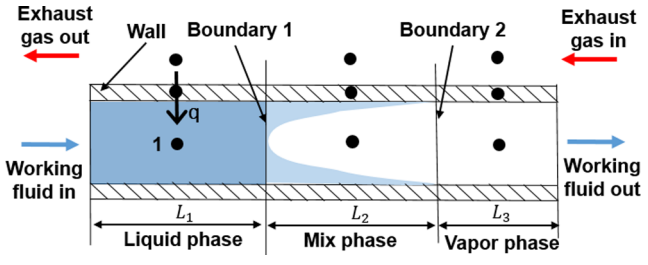

Fig. 3. Schematic of moving boundary model in a counter-flow scenario.

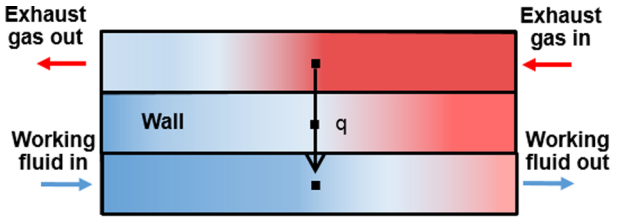

Fig. 4. Schematic of 0-D lumped model in a counter-flow scenario.

2.4. Heat transfer coefficients

The heat transfer coefficient between the exhaust gas and the working fluid tube wall is equivalent and it holds true for all three models. Thus, each of the FVM and MBM utilizes the same exhaust gas heat transfer coefficient expression as the 0-D lumped model due to the fast dynamics of exhaust gas. The heat exchanger is in helical coil type, which is provided by the project sponsor. The benefits of helical coil heat exchanger are improved thermal efficiency, compactness, ease of manufacture and maintenance, and enhanced heat convection [42]. The helical coil is placed inside a large concentric tube type heat exchanger and locates between two concentric tubes. Working fluid flows inside the helical coil and exhaust gas flows in the space between the two concentric tubes. The heat exchanger type affects the correlations of the heat transfer coefficients based on the key parameters of heat exchangers, such as the shape and length of flow path in the heat source side and working fluid side. The longer the flow path is, the longer time the fluid stays in the heat \exchanger and the longer time for the heat transfer. The thin flow path increases the heat transfer coefficient compared with the wide flow path [43], which leads to many researches in micro channel heat transfer [44,45]. The correlations of different types of heat exchangers can be found in [46]. In this study, the heat transfer coefficient between the exhaust gas and the working fluid tube wall is calculated as follows [47]:

$$U_{gw} = Nu\frac{m_U k_g}{d_{shelleqv}} \tag{21}$$

The structure of the evaporator modeled herein differs slightly from concentric tubes as the helical coil is inserted between the tubes, so a heat transfer coefficient multiplier (m_U) is applied and will be identified with experimental data. The parameters used in Eq. (21) are calculated as follows:

$$Nu = \frac{\left(\frac{\xi_g}{8}\right)Re_g Pr_g}{K_g + 12.7\sqrt{\frac{\xi_g}{8}}\left(Pr_g^{0.667} - 1\right)}\left[1 + \left(\frac{d_{shelleqv}}{L}\right)^{0.667}\right] \tag{21a}$$

$$K_g = 1.07 + \frac{900}{Re_g} - \frac{0.63}{(1 + 10\mathrm{Pr}_g)} \tag{21b}$$

$$Re_g = \frac{\dot{m}_g d_{shelleqv}}{A_{g,cross} v_d} \tag{21c}$$

$$Pr_g = \frac{v_d c_{pg}}{k_g} \tag{21d}$$

$$\xi_g = (1.8log_{10}(Re_g^*) - 1.5)^{-2} \tag{21e}$$

$$Re_g^* = Re_g\frac{(1 + r_d^2)ln(r_d) + (1 - r_d)}{(1 + r_d^2)ln(r_d)} \tag{21f}$$

$$r_d = \frac{d_{in}}{d_{out}} \tag{21g}$$

The Nusselt number expression of a concentric tube with an insulated outer pipe wall is selected based on the heat exchanger geometry [46]. The heat transfer coefficient on the working fluid side has a different format for each working fluid phase. Thus, the discretized modeling methodologies utilize a different heat transfer coefficient in each cell, which is both temporally and spatially dependent. The calculation of pure liquid and pure vapor heat transfer coefficients between the working fluid and the tube wall are given in Eq. (22). These heat transfer coefficients are selected according to the helical coil heat exchanger structure [46].

$$U_{fw,pure} = \frac{\left(\frac{\xi_f}{8}\right)Re_f Pr_f}{1 + 12.7\sqrt{\frac{\xi_f}{8}}\left(Pr_f^{0.667} - 1\right)}\frac{k_f}{d_f} \tag{22}$$

$$\xi_f = 0.0075\left(\frac{d_f}{D_f}\right)^{0.5} + \frac{0.079}{Re_f^{0.25}} \tag{22a}$$

The mixed-phase heat transfer coefficient between the working fluid and the tube wall is calculated from a vertical tube two-phase heat transfer coefficient expression [46], which shares a similar structure with the tube-shell utilized in the experiments. $U_{fw,l}$ and $U_{fw,v}$ are calculated using single phase Eq. (22). The mixed-phase heat transfer coefficient is expressed as follows:

$$U_{fw,mix} = \left\{(1 - x)^{0.01}\left[(1 - x) + 1.9x^{0.4}\left(\frac{\rho_{f,l}}{\rho_{f,v}}\right)^{0.35}\right]^{-2.2} + x^{0.01}\left[\frac{U_{fw,v}}{U_{fw,l}}\left(1 + 8(1 - x)^{0.7}\left(\frac{\rho_{f,l}}{\rho_{f,v}}\right)^{0.67}\right)\right]^{-2}\right\}^{-0.5} \tag{23}$$

Between the working fluid and the tube wall, the heat transfer coefficient expressions are different based on different working fluid phases. For the FVM, the working fluid phase of the cell is determined from working fluid quality, x, as follows:

$$phase_{FVM} = \begin{cases} pureliquid, & ifx \le 0 \\ liquid\&vapormix, & if0 < x < 1 \\ purevapor, & ifx \ge 1 \end{cases} \tag{24}$$

$$x = \frac{h_f - h_{f,l}}{h_{f,v} - h_{f,l}} \tag{24a}$$

About how the discretization is defined for MBM, the working fluid phase in each cell is known. Pure liquid exists in cell #1, mixed phase in cell #2, and pure vapor in cell #3.

For the 0-D lumped model, there is only one heat transfer coefficient expression and it is the average heat transfer coefficient from all three phases as shown in Eq. (25). The pure liquid and pure vapor heat transfer coefficients terms in Eq. (25) are calculated using Eq. (22). The mixed-phase heat transfer coefficient term is calculated using Eq. (23) by setting vapor quality $x = 0.5$.

$$U_{fw,0D} = \frac{1}{3}U_{fw,pureliquid} + \frac{1}{3}U_{fw,mix} + \frac{1}{3}U_{fw,purevapor} \tag{25}$$

3. Model comparison

Experimental data are required in the model validation. In this study, experiments are conducted in the heavy-duty powertrain lab in Clemson University Department of Automotive Engineering. The engine is a 13L heavy-duty diesel engine with 353 kW rated power. The engine torque and power are achieved by close-loop control of fueling rate, EGR valve, and throttle. The working fluid vapor temperature is controlled via the working fluid pump. Working fluid pressure is controlled via the turbine bypass valve. The condenser is cooled down by the building cooling water and the cooling water is set at the maximum flow rate. During the engine and ORC-WHR system warm up, the working fluid pump and turbine bypass valve are set at fixed position.

Once the vapor appears at the evaporator outlet, PID feedback and feedforward controls are activated in both working fluid pump and turbine bypass valve to control the vapor temperature and evaporation pressure, respectively. When the system shifts from one steady state condition to the other one, the PID feedback and feedforward controls are active until the steady state condition are reached. The data is then collected for three minutes and all the parameters are processed with mean operation. Thus, only single value from each parameter represents the steady state condition. In the transient test, the controls are active. As shown Fig. 5, the ORC-WHR system considers TP exhaust as the heat source. The experiments setup is based on the optimal design point and actual system conditions that the ORC-WHR will operate in the vehicle driving. The engine operating conditions cover the most frequent condition of a long haul truck running in high way. The heat exchanger design are optimized based on the least pressure drop in both working fluid and exhaust gas sides, and the working fluid design evaporation pressure and vapor temperature. The working fluid temperature at evaporator inlet also matches the best performance in the condenser. The experiments are conducted at multiple steady state engine conditions and the measured parameters are shown in Table 1. Among the steady state engine operating conditions, the exhaust gas mass flow rate is in the range of 0.18–0.4 kg/s, and the exhaust gas temperature is in the range of 312–350 °C. The heavy-duty engine operating points vary from 1200 rpm/1000 Nm to 1600 rpm/1400 Nm, which is a wide range for the typical heavy-duty diesel engine in long haul trucks. In the exhaust gas side, temperature is measured both at evaporator inlet and outlet. Mass flow rate is calculated based on intake air mass flow measurement. In the working fluid side, temperature and pressure are measured at evaporator inlet and outlet. Working fluid mass flow rate is measured at the evaporator inlet. Further details of the experiments setup can be found in [18].

Ethanol is utilized as the working fluid, which is provided by sponsor. Compared with other working fluids, ethanol has high thermal efficiency. Teng et al. concluded that Ethanol can be an alternative for R245fa for the ORC-WHR application [48]. According to the screening of 72 million working fluids in study [49], ethanol is ranked No.1 for the mobile ORC application. Besides ethanol, other common working fluids are R245fa [50], R123zd(E) [51,52], and CO_2 [26,53]. Besides pure working fluid, fluid mixtures also attract researchers' attention. Teng et al. analyzed the general benefits and drawbacks of fluid mixtures [54]. The study concluded that the binary fluid has a higher evaporator outlet temperature than any of pure fluids that used in the binary fluids and help increase the thermal efficiency. However, the disadvantage of binary fluids is that the lowest boiling point fluid element vaporizes at the initial evaporation phase and floats on top entering the expander. Up to 15% improvement in the thermal efficiency can be achieved by the binary fluid in comparison to pure fluids. Besides the efficiency improvement, fluid mixtures can be created for the flammability suppression by adding CO_2. For example, Garg et al. conducted the flammability study on the CO_2 mixtures of isopentane and propane [55]. Working fluid selection requires systematic analysis, which considers the heat source mass flow rate and temperature, heat exchanger structure and materials, cooling capacity and temperature of cooling fluid, and expander type. The modeling equations in the entire Section 2 do not change as working fluid changes. Only the thermodynamic tables change when different working fluids are utilized. If the heat exchanger type changes, all the equations in Sections 2.1, 2.2 and 2.3 do not change. Only the heat transfer coefficients in Section 2.4 change and the equation forms should match the structure of the heat exchanger, such as the shape and length of the flow path in both exhaust gas side and working fluid side. Working fluid selection is not the focus of this study, thus selection details are not included. Further information of working fluid selection for the ORC-WHR system can be found in [56–58].

To minimize the measurement noise and uncertainty in the experiments, multiple factors are carefully considered. In the sensor and actuator selection, high accuracy is one of the key standards. Take thermal couples as an example, 1/16 in. diameter thermal couple reduces response time when compared to 1/4 in. diameter thermal couple. It was found in experiments that the measured temperature difference could be as large as 10 K during the ORC transient conditions. In the sensor and actuation installation, the location, diameter of the flow path, depth of the sensor in the pipe strictly follow the installation manual. In the experiments, it was found that the different installation of engine intake air mass flow sensor could cause as large as 5% measurement difference. The ORC-WHR system are separated from the engine vibration by the flexible hose connected the aftertreatment system and the TP heat exchanger. In addition, cushions are added to the working fluid pump motor mounting point to reduce vibration. The imc data acquisition hardware is chosen to minimize the uncertainty from hardware. Controller Area Network (CAN) bus is utilized for the signal transmission. To reduce the measurement noise from Electromagnetic Compatibility (EMC) problem, the twisted wires are used. The CAN nodes connection and location of termination resistors strictly follow the CAN bus setup standard.

The rest of this section is organized as follows:

i. The three models are identified using the same aforementioned experimental dataset.
ii. The vapor temperature dynamics performance are compared in an engine step change condition.
iii. The overall model accuracy (i.e. steady state accuracy plus transient accuracy) is evaluated over two set of experimental data with transient engine conditions.
iv. Model computation cost is compared.
v. Modeling effort (i.e. the amount of modeling time) is compared.

3.1. Model identification

This section identifies the heat exchanger efficiency multiplier m_η (in Eqs. (7), (11), (14), and (17)) and the heat transfer coefficient multiplier m_U (in Eq. (21)) using steady state experimental data. These two identification parameters correct the error introduced by discretization of three models and the slightly difference between actual heat exchanger and concentric tubes, where the empirical Nusselt number expression is derived from. Different models share the geometry parameters of the heat exchanger. First, the two parameters are optimized individually in each steady state operating point using Particle Swarm Optimization (PSO) method [59]. The optimized parameters are then plotted as the x axis in Fig. 6. Then the individual pairs

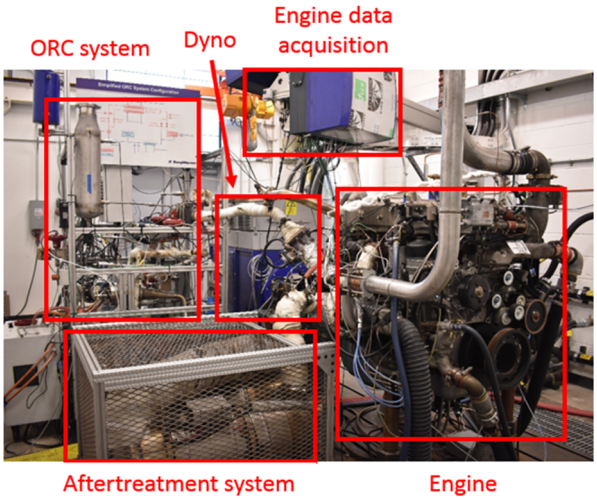

Fig. 5. ORC-WHR system in the test rig. TP evaporator locates downstream of aftertreatment system.

Table 1
Steady state conditions collected in tests.

	Unit	1	2	3	4	5	6	7	8
Engine speed	rpm	1200	1300	1300	1300	1400	1600	1600	1600
Engine torque	Nm	1000	1100	1100	1300	1200	1300	1400	1350
Engine fuel rate	g/s	25	29.3	28.8	34.1	33.5	42.0	45.0	43.4
$\dot{m}_{g,in}$	kg/s	0.18	0.23	0.23	0.27	0.33	0.34	0.38	0.4
$T_{g,in}$	°C	344	344	330	330	330	312	317	350
$\dot{m}_{f,in}$	kg/s	0.019	0.022	0.022	0.025	0.032	0.030	0.034	0.04
$T_{f,in}$	°C	27	26	30	30	27	30	27	32

of (m_η, m_U) are fitted with second order polynomial equations with exhaust gas mass flow rate and temperature as equation inputs as shown in Eqs. (26) and (27). Given exhaust gas mass flow rate and temperature, the correlations then predict the pair of (m_η, m_U), which are presented as the y axis in Fig. 6. The same identification process is conducted in all three heat exchanger models. Details of the heat exchanger identification processes are presented in [18]. The identification results are shown in Fig. 6. The six subplots in Fig. 6 try to show the prediction accuracy of the correlations in Eqs. (26) and (27). The x axis represents the true values of efficiency and heat transfer coefficient multiplier from experiments, while the y axis represents the predicted values using the correlations. All three models use the same correlation and the only difference is the calibration parameters in those correlations (i.e., a_1, a_2, $\cdots$, a_6, b_1, b_2, $\cdots$, b_6). Each dot represents one steady state condition. The line across the diagonal is the 45° line. The closer the dot is to the 45° line, the better prediction accuracy the correlation has. The multipliers from the experiments are obtained using Particle Warm Optimization (PSO) in the model simulation given experimental data as input.

$$m_\eta = a_1 + a_2\dot{m}_g + a_3 T_g + a_4\dot{m}_g^2 + a_5\dot{m}_g T_g + a_6 T_g^2 \tag{26}$$

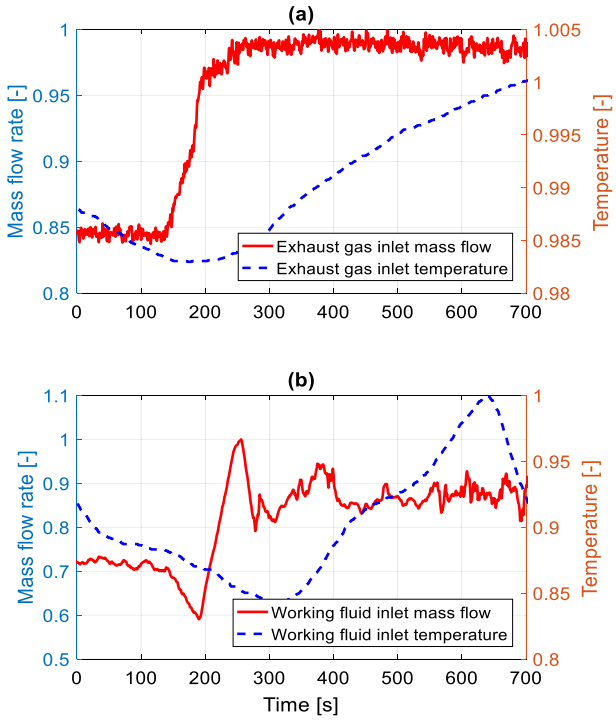

Fig. 7. Experimental measured inputs utilized in working fluid vapor temperature dynamics comparison. (All values are normalized by their respective maximum absolute value.)

$$m_U = b_1 + b_2\dot{m}_g + b_3 T_g + b_4\dot{m}_g^2 + b_5\dot{m}_g T_g + b_6 T_g^2 \tag{27}$$

3.2. Vapor temperature dynamic performance

The model accuracy is first evaluated by the model dynamic performance. In this evaluation, the engine speed and load step change.

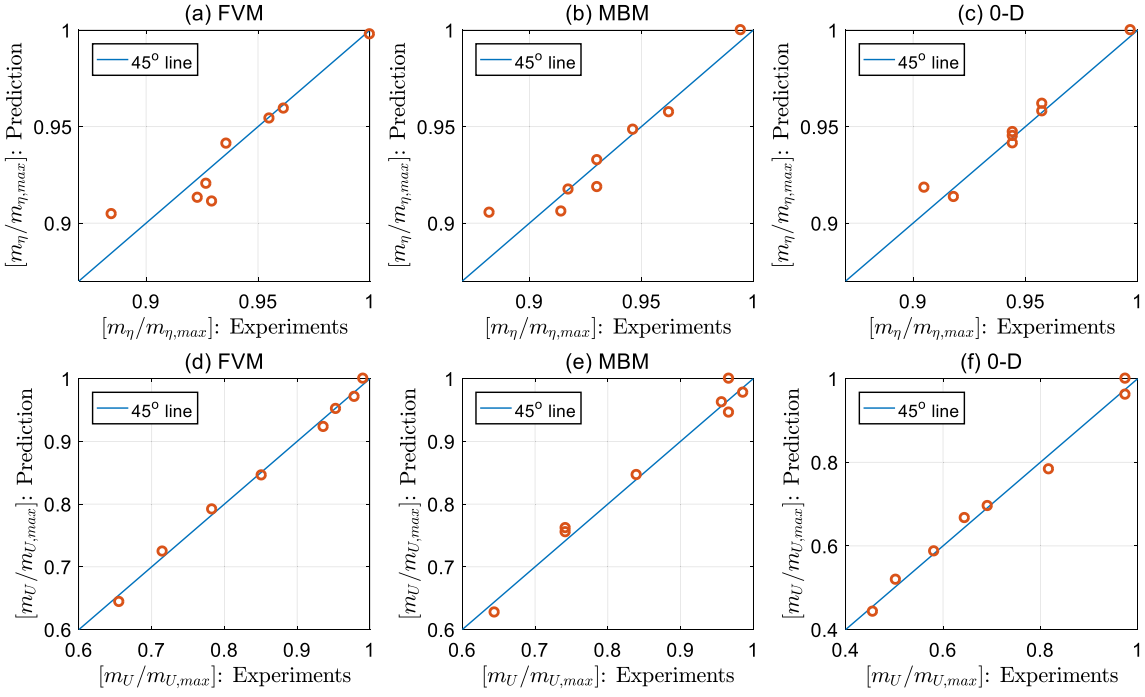

Fig. 6. Multipliers comparison between experimental results (obtained using PSO parameter identification) and correlation prediction results for three heat exchanger models. (a), (b), (c) FVM, MBM, 0-D lumped model efficiency multiplier, respectively, (d), (e), (f) FVM, MBM, 0-D lumped model heat transfer coefficient multiplier, respectively. In each plot, the values are normalized by the maximum value in the respective plot.

The evaporator models are identified based on the two steady state conditions at either end of the step change. Then the two sets of identified heat transfer coefficient multipliers and evaporator efficiency multipliers are utilized based on the exhaust gas mass flow rate change trend during the step change as shown in Fig. 7(a). The working fluid temperature comparison is shown in Fig. 8 with the FVM using 30-cell discretization. The FVM and MBM have better alignment with experimental data than the 0-D lumped model. During 250–300 s, the MBM shows less dynamic response than the FVM, which increases the error during the transient and delays the MBM model response as noted in the peak at 230 s. The 0-D lumped model demonstrate significant phase advance compared to experimental data. Among the three models, the FVM shows the least phase error and transient error. The most noticeable observation in Fig. 8 is that the 0-D lumped model is too dynamic/fast relative to the experimental measurements, revealing that the minimized number of states does not capture the system dynamics.

The 0-D lumped model temperature dynamics can be slowed by adding inertia to the working fluid energy balance. The inertial multiplier $m_{inertia}$ is shown in Eq. (28). This modification only changes the working fluid enthalpy change rate and does not affect the steady state results as the term $\frac{dh_f}{dt}$ turns to zero at steady state. The modification accounts for the working fluid mass correction and transportation delay in the heat exchanger. As the mass term m_f contains the mass in all three phases (i.e., pure liquid, mixed and pure vapor working fluid), the single cell mass estimation may not be extremely accurate. Besides the mass correction, the inertial multiplier also plays a role to represent the transport delay in the 0-D model. For the FVM and MBM, which have three or more cells. The parameter changes at the inlet and outlet are not directly connected, but indirectly connected by the multiple cells. It takes time for the parameters change in the first cell to impact the last cell. However, in 0-D model, there is only single cell. The temperature variation in the cell, that results from the input changes, instantaneously and directly affects the output temperature without any cell in the middle as a buffer for the temperature change. Thus, the temperature response time in 0-D model is reduced due to the lack of transportation delay. The value of inertial multiplier is explored using grid search method in simulation and the representative results are plotted in Fig. 9. The inertia multiplier is swept from 1 to 50 by 1 at each step. As the inertia multiplier increases, the working fluid temperature dynamics slow down, reduce the phase advance and approach the experimental results. Based on the results of grid search, 18 is selected as the inertia multiplier as the 0-D model has the least temperature error during the transient.

$$m_{inertia} m_f \frac{dh_f}{dt} = \dot{m}_{f,in} h_{f,in} - \dot{m}_{f,out} h_{f,out} + A_{fw} U_{fw} (T_w - T_f) \tag{28}$$

3.3. Accuracy validation

With the identified correlations, the three models are validated over two sets of experimental data with transient engine conditions. The two transient conditions are plotted in Fig. 10 (Test 1) and Fig. 12 (Test 2). The results are shown in Figs. 11 and 13, respectively. Even though the FVM does not produce the least error at every instance of the data set, it has the overall best performance with respect to the dynamic trend and steady state error among the three models. During 1100–1600 s in Fig. 11 and 300–700 s in Fig. 13, FVM shows much less error than the MBM and modified 0-D model. In terms of dynamics, the FVM and modified 0-D model more closely reproduce the experimental data than the MBM. The large error shown in the MBM is the results of its slow dynamic response (300–500 s in Fig. 11 and 250–400 s in Fig. 13). In Fig. 13, the modified 0-D lumped model shows relatively large error compared with FVM and MBM.

The mean and maximum errors of these two tests are summarized in Table 2. The absolute value of the working fluid vapor temperature mean error are among 2–7 K, which is a quite acceptable range in the field of heavy-duty diesel ORC-WHR. The vapor temperature error percentage range is among 0.5–1.3%. The maximum errors are about three times of the mean error and the error percentage locates between 1.3% and 3.7%. In both tests, the FVM shows the least mean error. For the MBM and modified 0-D model, the error varies with tests. Overall, MBM and modified 0-D model present comparable accuracy when compared to FVM. Considering the good accuracy of modified 0-D, this model has the potential for all kinds of application purposes, which will be discussed later in this paper.

The mean/ max errors and error percentages are defined in Eqs. (29), (30), (31), and (32). N in the equations means the number of time step and subscripts sim, exp represent simulation and experiments, respectively.

$$e_{mean} = \frac{1}{N} \sum_{i=1}^{N} |T_{sim}(t_i) - T_{exp}(t_i)| \tag{29}$$

$$e\_rate_{mean} = \frac{1}{N} \sum_{i=1}^{N} \frac{|T_{sim}(t_i) - T_{exp}(t_i)|}{T_{exp}(t_i)} \times 100\% \tag{30}$$

$$e_{max} = \max_t |T_{sim}(t) - T_{exp}(t)| \tag{31}$$

$$e\_rate_{max} = \max_t \frac{|T_{sim}(t) - T_{exp}(t)|}{T_{exp}(t)} \times 100\% \tag{32}$$

3.4. Computational cost

Model computation time is one of the most important performance parameters. Based on the software and language the modeling is built upon, the computation time is different. In this study, the models are all built and executed in Matlab R2017a version as m-script. The desktop utilized in the simulation comparison is Dell T3500 workstation with Intel Xeon W3530 2.80 GHz CPU and 8 GB RAM. To avoid repeatability, only Test 2 simulation time is compared in this section. The results are shown in Table 3. It turns out that the modified 0-D lumped model is six times faster than the MBM and twenty times faster than the 30-cell FVM. For the FVM, the computation time linearly increases with cell discretization.

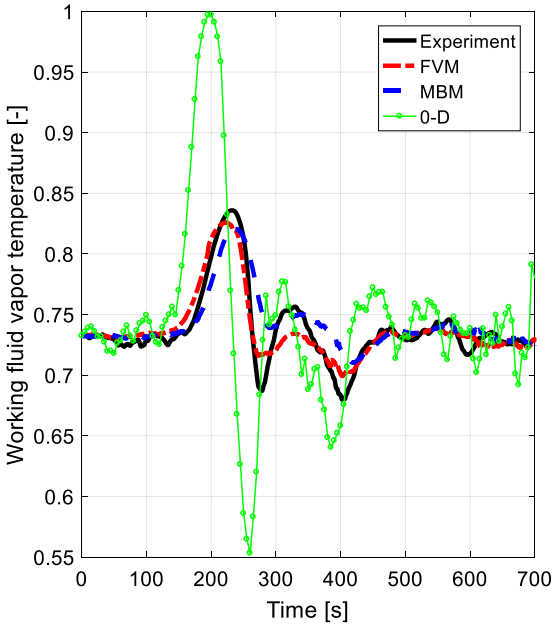

Fig. 8. Working fluid vapor temperature dynamics comparison among three evaporator models and experimental data. (All values are normalized by their respective maximum absolute value.)

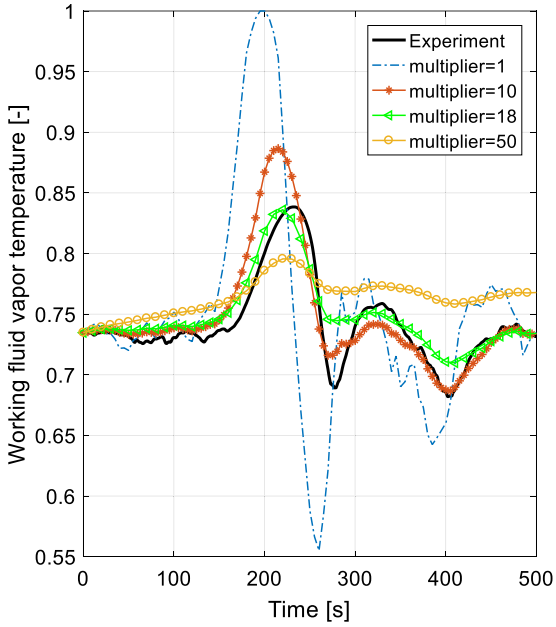

Fig. 9. 0-D lumped model response results with different working fluid inertia multipliers. (All values are normalized by their respective maximum absolute value.)

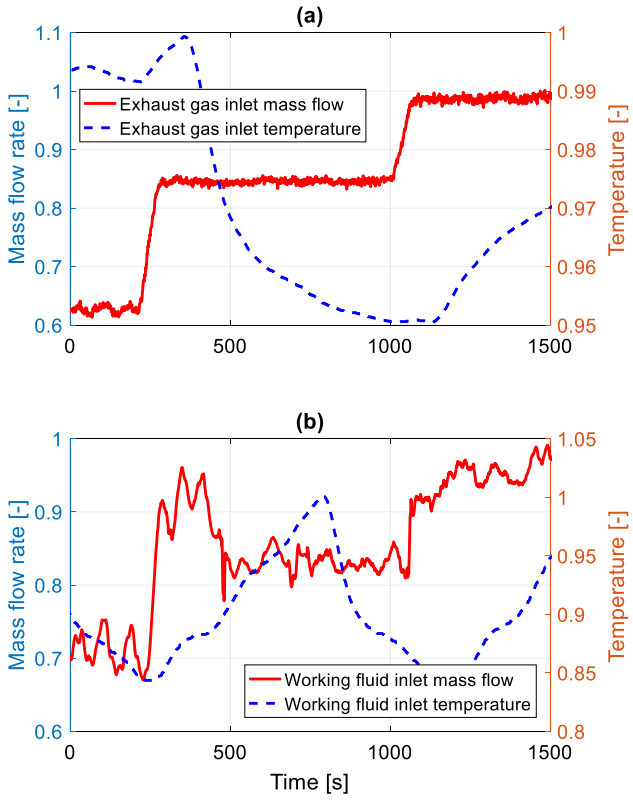

Fig. 10. Experimental measured inputs utilized in working fluid vapor temperature accuracy comparison – Test 1. (All values are normalized by their respective maximum absolute value.)

3.5. Modeling effort

In the software development, the number of lines of code is utilized as the metric to assess the modeling effort [60]. Different from general software development, in the heat exchanger model development, most of time is spent on deriving the governing equations, rather than coding

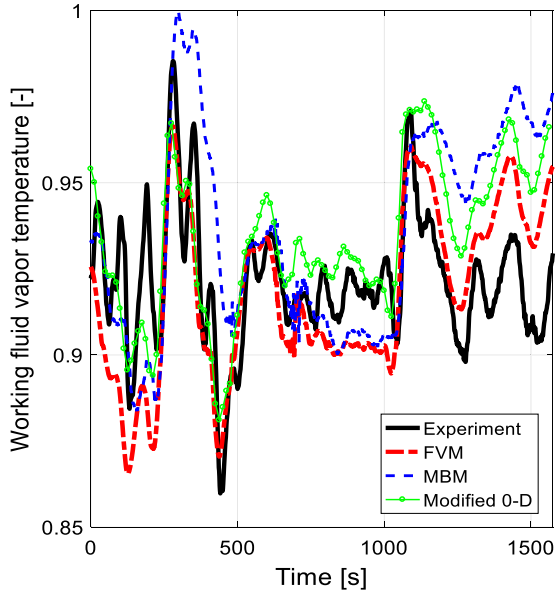

Fig. 11. Working fluid vapor temperature accuracy comparison among three evaporator models and experimental data – Test 1. (All values are normalized by their respective maximum absolute value.)

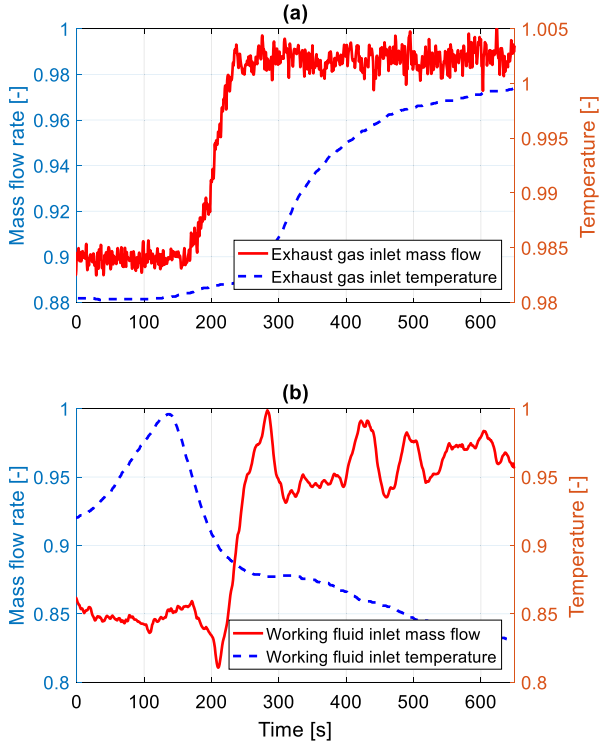

Fig. 12. Experimental measured inputs utilized in working fluid vapor temperature accuracy comparison – Test 2. (All values are normalized by their respective maximum absolute value.)

the model in the Matlab. Thus, the number of lines of code does not fit this problem. In hardware 3D design, number of components/ objects was utilized as metric of modeling effort [61]. Similar to number of components, in this paper, the modeling effort is defined by the number of different equations as shown in Eq. (33). For the FVM, different cells share the same equations and only the variable values vary. In this case, no new equation derivation is required and no modeling effort is needed to expand the cell discretization from 1 to 30 or 100. Thus, FVM modeling effort is independent of the number of cells and it can be

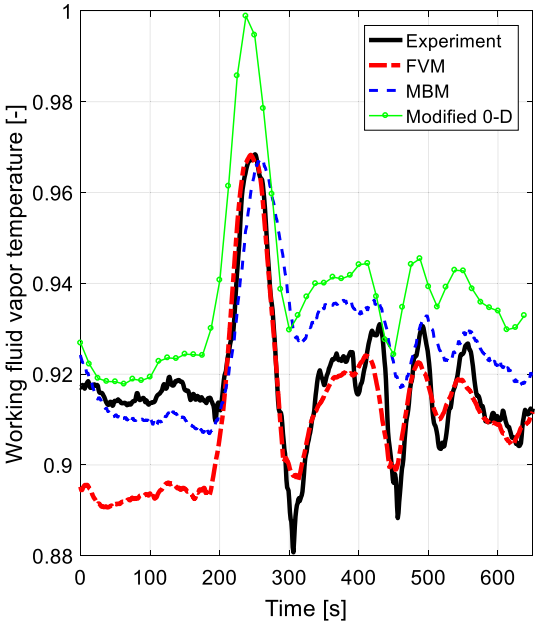

Fig. 13. Working fluid vapor temperature accuracy comparison among three evaporator models and experimental data – Test 2. (All values are normalized by their respective maximum absolute value.)

Table 2
Working fluid vapor temperature error comparison in two transient validation tests.

Model	30-cell FVM	MBM	Modified0-D model
Test 1 mean error [K]	4.5	6.6	5.1
Mean error percentage	0.87%	1.27%	0.98%
Test 1 max error [K]	17.1	17.3	18.7
Max error percentage	3.26%	3.42%	3.68%
Test 2 mean error [K]	2.6	3.0	5.2
Mean error percentage	0.50%	0.58%	1.00%
Test 2 max error [K]	7.0	13.0	12.9
Max error percentage	1.35%	2.56%	2.54%

Table 3
Model computation time comparison over Test 2 (test duration: 650 s).

Model	Computation time [s]
10-cell FVM	94.3
30-cell FVM	118.6
100-cell FVM	181.2
MBM	27.9
Modified 0-D lumped model	4.6

calculated based on 1-cell FVM (i.e. modified 0-D lumped model). Therefore, the modified 0-D lumped model has the same modeling effort as the FVM, which is 4 based on the governing Eqs. (5), (6), (7), and (8). The modeling effort of MBM is 12 based on the MBM governing equations through Eq. (9) to Eq. (20). The modeling effort results are summarized in Table 4.

$$ME = number\ \ of\ \ different\ \ equations \tag{33}$$

4. Model selection recommendation

The multiple phases of ORC-WHR system development may require different evaporator models based on the specific aims of each phase. This paper divides the development into six main phases from concept to experimental implementation as shown in the left side of Fig. 14. The concept phase in the ORC-WHR system development determines broad system parameters, such as system architecture, the number of heat sources, and the potential working fluids [62,63]. Then the component selection and development phase dives deeper to either develop components or select them from existing products on the market. After that, the components are integrated and connected into a complete system. In order to stably and safely operate the system, temperature and pressure controls are necessary. With the help of developed controls, power optimization is executed to fully explore the potential of the ORC-WHR system. Finally, experiments are conducted to validate the control and optimization results. Some of components may be upgraded based on the integrated system experimental performance relative to development goals. The discussion surrounding ORC-WHR model selection contained herein is based on different ORC-WHR system development phases as follows:

Concept phase: The main goals of the concept phase are roughly calculating the ORC-WHR system efficiency and evaluating different system architectures, heat sources, working fluids, etc. In general, there is no ORC-WHR experimental data in this phase and the model accuracy requirement is not high. The modified 0-D lumped model provides both moderate accuracy and the least modeling effort, satisfying the requirements of the evaporator model in this phase. The additional model development effort of the MBM and the high computation cost of the FVM are not necessary in the concept phase.

Components selection and development phase: The main goals of this phase are developing the main components (e.g. evaporators and expander) and selecting the required accessory components (e.g. pump, valves, pipes, etc.). In the component design phase, model accuracy is the most important factor. Computation time and modeling effort can be compromised. Therefore, a FVM model is the first choice for the component development phase because of its high accuracy [18]. The appropriate FVM discretization can be determined based on requirements of accuracy and computation cost in each specific design. The number of cells can be increased until the satisfactory accuracy is attained.

Control development phase: The main goals of the control development phase are building controls for the working fluid vapor temperature and pressure regulation. Even though PID feedback control is capable of controlling an ORC-WHR system at steady state engine operating conditions, PID exhibits compromised performance during transient engine conditions [40,64]. It was reported that model-based controls showed better temperature tracking performance than PID feedback control for ORC-WHR systems [20]. In mode-based control, the evaporator model should possess low state dimension and moderate accuracy to facilitate both real-time execution of the model-based control while ensuring valid results. Model-based controls will struggle if model error is significant.

Based on the two requirements in the model-based control development, the MBM and modified 0-D lumped method are both suitable choices. The MBM has lower computation cost than the FVM as shown in Table 3, and it has moderate accuracy. The modified 0-D lumped model has the least computation cost and has similar accuracy to the MBM. If control development time is very limited or the computation cost requirement is the most important factor, modified 0-D lumped model is the first choice. If development time is not a concern and the computation cost requirement is relaxed, then the MBM provides a physics-based advantage for operation beyond the calibration data sets.

Table 4
Modeling effort comparison.

Model	Modeling effort [-]
10-cell FVM	4
30-cell FVM	4
100-cell FVM	4
MBM	12
Modified 0-D lumped model	4

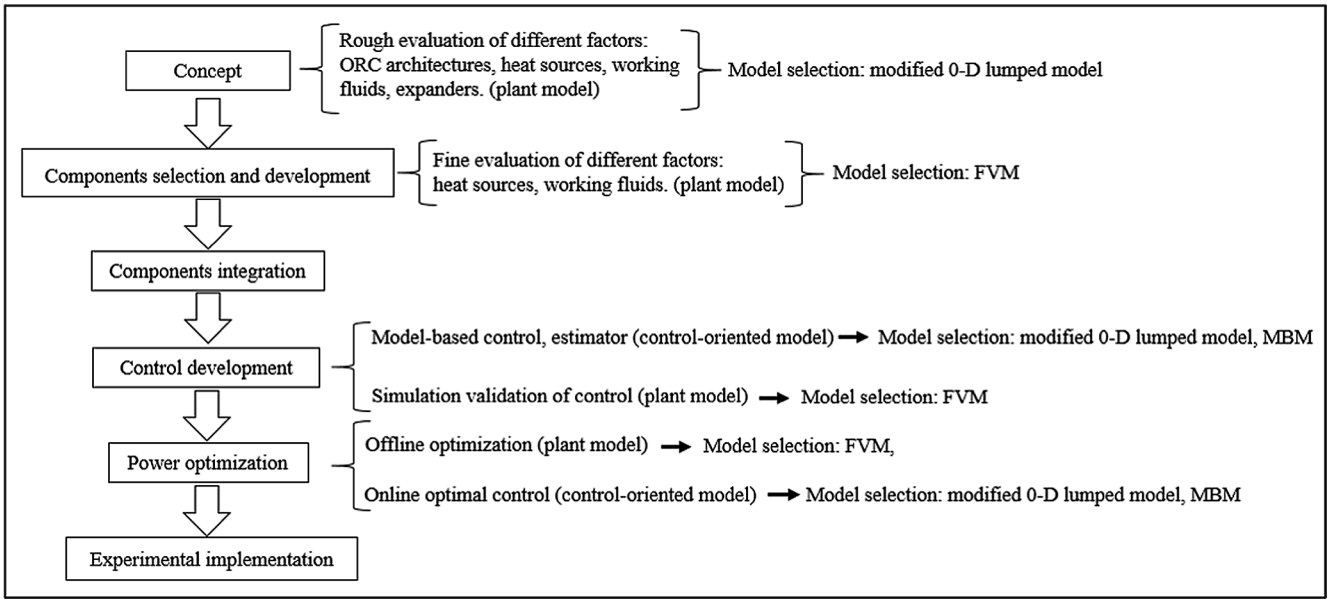

Fig. 14. Model selection recommendation by ORC-WHR system development phases.

Recall that the multiplier added in 0-D model is not physical while MBM is built upon physics-based governing equations.

To validate control performance in the simulation environment, the plant model must be very accurate. Thus, FVM is the first choice for the plant model. In addition, utilization of a different model for the plant and controller facilitates verification of the model-based controller model error and disturbance rejection capability.

Power optimization phase: The main goals of power optimization phase are maximizing the net power output from the ORC-WHR system (i.e. improve the expander power production and reduce the working fluid pump and coolant pump power consumption). The power optimization can be conducted offline or online. When conducted offline, the power optimization generates correlations among the heat source mass flow rate, heat source temperature, working fluid optimal superheat temperature, working fluid optimal evaporating pressure, working fluid condensation pressure, etc. [23]. These correlations are either fitted in equations or saved in lookup tables before implementation in the real system [65]. In this offline optimization, model accuracy is most important and the computation time is not restricted. Thus, the FVM is the first choice.

5. Conclusion

This paper presents an ORC-WHR evaporator modeling comparison considering finite volume model, moving boundary model and 0-D lumped evaporator model. Accuracy, computation time, and modeling effort are investigated. A detailed description of each modeling methodology and the experimental identification are provided. This paper first time compares the three popular models using the same set of identification parameters and experimental data. Based on the transient validation results, all three models show decent working fluid vapor temperature prediction accuracy as the mean error is less than 6.6 K and the mean error percentage is less than 1.27%. The maximum error is bounded within 19 K or 3.7%.

The 0-D lumped model shows substantial accuracy improvement after adding a mass multiplier in the working fluid energy balance equation to calibrate the temperature dynamic response. After the calibration, the 0-D lumped model accuracy is on par with the moving boundary model and only slightly worse than the finite volume model. Considering that the 0-D lumped model possesses the lowest state dimension of the three methodologies, the high accuracy modified 0-D model can be utilized in many different purposes from optimization to control.

Even though eight steady state points and two transient tests are considered in the model identification and validation, respectively, the amount of experimental data is still limited. In the future, more experimental data should be collected both in steady state and transients to further validate the accuracy of the three models.

Declaration of Competing Interest

None.

References

[1] T. Park, Teng, H., Hunter, G. L., Velde B. V. D. and Klaver, J., "A Rankine Cycle System for Recovering Waste Heat from HD Diesel Engines - Experimental Results," SAE International 2011-01-1337, 2011.
[2] T.A. Horst, W. Tegethoff, P. Eilts, J. Koehler, Prediction of dynamic Rankine cycle waste heat recovery performance and fuel saving potential in passenger car applications considering interactions with vehicles' energy management, Energy Convers. Manage. 78 (2014) 438–451.
[3] T. Endo, S. Kawajiri, Y. Kojima, K. Takahashi, T. Baba, S. Lbaraki, T. Takahashi, M. Shinohara, Study on maximizing exergy in automotive engines, SAE Tech. Paper (2007).
[4] S. Ahmadi Atouei, A.A. Ranjbar, A. Rezania, Experimental investigation of two-stage thermoelectric generator system integrated with phase change materials, Appl. Energy 208 (2017) 332–343.
[5] M.K. Altstedde, F. Rinderknecht, H. Friedrich, Integrating phase-change materials into automotive thermoelectric generators, J. Electron. Mater. 43 (2014) 2134–2140.
[6] R. Patowary, D.C. Baruah, Thermoelectric conversion of waste heat from IC engine-driven vehicles: a review of its application, issues, and solutions, Int. J. Energy Res. 42 (2018) 2595–2614.
[7] H. Aghaali, H.E. Aringngstrom, A review of turbocompounding as a waste heat recovery system for internal combustion engines, Renew. Sustain. Energy Rev. 49 (2015) 813–824.
[8] M. Kant, A. Romagnoli, A.M.I. Mamat, R.F. Martinez-Botas, Heavy-duty engine electric turbocompounding, Proceedings of the Institution of Mechanical Engineers Part D-Journal of Automobile Engineering, 2015, pp. 457–472.
[9] G. He, H. Xie, S. He, Overall efficiency optimization of controllable mechanical turbo-compounding system for heavy duty diesel engines, Sci. China Technol. Sci. 60 (2017) 36–50.
[10] M. Astolfi, M.C. Romano, P. Bombarda, E. Macchi, Binary ORC (Organic Rankine Cycles) power plants for the exploitation of medium low temperature geothermal sources - part B: techno-economic optimization, Energy 66 (2014) 435–446.
[11] J. Sun, W.H. Li, Operation optimization of an organic Rankine cycle (ORC) heat recovery power plant, Appl. Therm. Eng. 31 (2011) 2032–2041.
[12] X.Y. Li, H. Tian, G.Q. Shu, M.R. Zhao, C.N. Markides, C. Hu, Potential of carbon dioxide transcritical power cycle waste-heat recovery systems for heavy-duty truck engines, Appl. Energy 250 (2019) 1581–1599.

[13] X.Y. Li, H. Tian, G.Q. Shu, C. Hu, R. Sun, L.G. Li, Effects of external perturbations on dynamic performance of carbon dioxide transcritical power cycles for truck engine waste heat recovery, Energy 163 (2018) 920–931.

[14] F. Willems, F. Kupper, G. Rascanu, E. Feru, Integrated energy and emission management for diesel engines with waste heat recovery using dynamic models, Oil Gas Sci. Technol.-Revue D Ifp Energ. Nouvelles 70 (2015) 143–158.

[15] B. Xu, D. Rathod, A. Yebi, Z. Filipi, A Comparative analysis of real-time power optimization for organic Rankine cycle waste heat recovery systems, Appl. Therm. Eng. (2019) 114442.

[16] D. Seher, T. Lengenfelder, J. Gerhardt, N. Eisenmenger, M. Hackner, I. Krinn, Waste heat recovery for commercial vehicles with a Rankine process, 21st Aachen Colloquium on Automobile and Engine Technology, Aachen, Germany, 2012, pp. 7–9.

[17] D. Koeberlein, "Cummins SuperTruck Program Technology and System Level Demonstration of Highly Efficient and Clean, Diesel Powered Class 8 Trucks," presentation at US Department of Energy Merit Review, 2013.

[18] B. Xu, D. Rathod, S. Kulkarni, A. Yebi, Z. Filipi, S. Onori, et al., Transient dynamic modeling and validation of an organic Rankine cycle waste heat recovery system for heavy duty diesel engine applications, Appl. Energy 205 (2017) 260–279.

[19] D.H. Wei, X.S. Lu, Z. Lu, J.M. Gu, Dynamic modeling and simulation of an organic Rankine cycle (ORC) system for waste heat recovery, Appl. Therm. Eng. 28 (2008) 1216–1224.

[20] A. Yebi, B. Xu, X. Liu, J. Shutty, P. Anschel, Z. Filipi, et al., Estimation and predictive control of a parallel evaporator diesel engine waste heat recovery system, IEEE Trans. Control Syst. Technol. (2017) 1–14.

[21] A. Hernandez, A. Desideri, S. Gusev, C.M. Ionescu, M. Van Den Broek, S. Quoilin, et al., Design and experimental validation of an adaptive control law to maximize the power generation of a small-scale waste heat recovery system, Appl. Energy 203 (2017) 549–559.

[22] B. Xu, A. Yebi, S. Onori, Z. Filipi, X. Liu, J. Shutty, et al., Transient power optimization of an organic Rankine cycle waste heat recovery system for heavy-duty diesel engine applications, SAE Int. J. Alternat. Powertrains 6 (2017) 25–33.

[23] S. Quoilin, R. Aumann, A. Grill, A. Schuster, V. Lemort, H. Spliethoff, Dynamic modeling and optimal control strategy of waste heat recovery organic Rankine cycles, Appl. Energy 88 (2011) 2183–2190.

[24] D. Junqi, Z. Xianhui, W. Jianzhang, Experimental study on thermal hydraulic performance of plate-type heat exchanger applied in engine waste heat recovery, Arab. J. Sci. Eng. 43 (2018) 1153–1163.

[25] A.P. Weiß, T. Popp, J. Müller, J. Hauer, D. Brüggemann, M. Preißinger, Experimental characterization and comparison of an axial and a cantilever microturbine for small-scale organic Rankine cycle, Appl. Therm. Eng. 140 (2018) 235–244.

[26] X.Y. Li, G.Q. Shu, H. Tian, G.D. Huang, P. Liu, X. Wang, et al., Experimental comparison of dynamic responses of CO2 transcritical power cycle systems used for engine waste heat recovery, Energy Convers. Manage. 161 (2018) 254–265.

[27] D. Rathod, B. Xu, Z. Filipi, M. Hoffman, An experimentally validated, energy focused, optimal control strategy for an organic rankine cycle waste heat recovery system, Appl. Energy (2019).

[28] V. Grelet, T. Reiche, L. Guillaume, and V. Lemort, "Optimal waste heat recovery Rankine based for heavy duty applications," 2014.

[29] M. Yousefzadeh, E. Uzgoren, Mass-conserving dynamic organic Rankine cycle model to investigate the link between mass distribution and system state, Energy 93 (2015) 1128–1139.

[30] B. Xu, A. Yebi, M. Hoffman, S. Onori, A rigorous model order reduction framework for waste heat recovery systems based on proper orthogonal decomposition and galerkin projection, IEEE Trans. Control Syst. Technol. (2018).

[31] E. Feru, F. Willems, B. de Jager, M. Steinbuch, Model predictive control of a waste heat recovery system for automotive diesel engines, Proceedings of the 18th International Conference on System Theory, 2014, pp. 658–663.

[32] J. Peralez, P. Tona, O. Lepreux, A. Sciarretta, L. Voise, P. Dufour, et al., Improving the Control Performance of an Organic Rankine Cycle System for Waste Heat Recovery from a Heavy-Duty Diesel Engine using a Model-Based Approach, 2013 Ieee 52nd Annual Conference on Decision and Control (Cdc), 2013, pp. 6830–6836.

[33] G. Hou, S. Bi, M. Lin, J. Zhang, J. Xu, Minimum variance control of organic Rankine cycle based waste heat recovery, Energy Convers. Manage. 86 (2014) 576–586.

[34] T.A. Horst, H.S. Rottengruber, M. Seifert, J. Ringler, Dynamic heat exchanger model for performance prediction and control system design of automotive waste heat recovery systems, Appl. Energy 105 (2013) 293–303.

[35] D. Di Battista, M. Di Bartolomeo, C. Villante, R. Cipollone, On the limiting factors of the waste heat recovery via ORC-based power units for on-the-road transportation sector, Energy Convers. Manage. 155 (2018) 68–77.

[36] H.X. Chen, W.L. Zhuge, Y.J. Zhang, T. Chen, L. Zhang, Performance Simulation of an Integrated Organic Rankine Cycle and Air Inter-Cooling System for Heavy-Duty Diesel Truck Engines, Proceedings of the Asme Turbo Expo: Turbine Technical Conference and Exposition, 2017, (2017).

[37] G.Q. Shu, X.N. Li, H. Tian, X.Y. Liang, H.Q. Wei, X. Wang, Alkanes as working fluids for high-temperature exhaust heat recovery of diesel engine using organic Rankine cycle, Appl. Energy 119 (2014) 204–217.

[38] J. Peralez, P. Tona, A. Sciarretta, P. Dufour, M. Nadri, Optimal control of a vehicular organic rankine cycle via dynamic programming with adaptive discretization grid, IFAC Proc. Vol. 47 (2014) 5671–5678.

[39] A. Desideri, B. Dechesne, J. Wronski, M. van den Broek, S. Gusev, V. Lemort, et al., Comparison of moving boundary and finite-volume heat exchanger models in the modelica language, Energies 9 (2016).

[40] A. Yebi, B. Xu, X. Liu, J. Shutty, P. Anschel, S. Onori, et al., Nonlinear Model Predictive Control Strategies for a Parallel Evaporator Diesel Engine Waste Heat Recovery System, ASME 2016 Dynamic Systems and Control Conference, (2016).

[41] T.A. Horst, W. Tegethoff, P. Eilts, J. Koehler, Prediction of dynamic Rankine cycle waste heat recovery performance and fuel saving potential in passenger car applications considering interactions with vehicles' energy management, Energy Convers. Manage. 78 (2014) 438–451.

[42] J. Fernández-Seara, C. Piñeiro-Pontevedra, J.A. Dopazo, On the performance of a vertical helical coil heat exchanger. Numerical model and experimental validation, Appl. Therm. Eng. 62 (2014) 680–689.

[43] W.L. Qu, I. Mudawar, Flow boiling heat transfer in two-phase micro-channel heat sinks - I. Experimental investigation and assessment of correlation methods, Int. J. Heat Mass Transf. 46 (2003) 2755–2771.

[44] L.A. Jiang, M. Wong, Y. Zohar, Forced convection boiling in a microchannel heat sink, J. Microelectromech. Syst. 10 (2001) 80–87.

[45] S.M. Kim, I. Mudawar, Thermal design and operational limits of two-phase microchannel heat sinks, Int. J. Heat Mass Transf. 106 (2017) 861–876.

[46] V. H. Atlas, "VDI-Gesellschaft Verfahrenstechnik und Chemieingenieurwesen (GVC)," in Ch. Part D-Thermophysical Properties, ed: Springer-Verlag, Berlin/Heidelberg Germany, 2010, pp. 121–613.

[47] T.L. Bergman, F.P. Incropera, A.S. Lavine, Fundamentals of Heat and Mass Transfer, John Wiley & Sons, 2011.

[48] H. a. R. Teng, G., "Improving Fuel Economy for HD Diesel Engines with WHR Rankine Cycle Driven by EGR Cooler Heat Rejection," SAE International 2009-01-2913, 2009.

[49] M. Preissinger, J.A.H. Schwobel, A. Klamt, D. Bruggemann, Multi-criteria evaluation of several million working fluids for waste heat recovery by means of organic Rankine cycle in passenger cars and heavy-duty trucks, Appl. Energy 206 (2017) 887–899.

[50] G.Q. Shu, M.R. Zhao, H. Tian, Y.Z. Huo, W.J. Zhu, Experimental comparison of R123 and R245fa as working fluids for waste heat recovery from heavy-duty diesel engine, Energy 115 (2016) 756–769.

[51] S. Eyerer, C. Wieland, A. Vandersickel, H. Spliethoff, Experimental study of an ORC (organic Rankine cycle) and analysis of R1233zd-E as a drop-in replacement for R245fa for low temperature heat utilization, Energy 103 (2016) 660–671.

[52] J.Y. Yang, Z.Y. Sun, B.B. Yu, J.P. Chen, Experimental comparison and optimization guidance of R1233zd(E) as a drop-in replacement to R245fa for organic Rankine cycle application, Appl. Therm. Eng. 141 (2018) 10–19.

[53] X.Y. Li, G.Q. Shu, H. Tian, L.F. Shi, G.D. Huang, T.Y. Chen, et al., Preliminary tests on dynamic characteristics of a CO2 transcritical power cycle using an expansion valve in engine waste heat recovery, Energy 140 (2017) 696–707.

[54] H. Teng, Regner, G. and Cowland, C., "Waste Heat Recovery of Heavy-Duty Diesel Engines by Organic Rankine Cycle Part II: Working Fluids for WHR-ORC," SAE Technical paper 2005-01-0543, 2007.

[55] P. Garg, P. Kumar, K. Srinivasan, P. Dutta, Evaluation of carbon dioxide blends with isopentane and propane as working fluids for organic Rankine cycles, Appl. Therm. Eng. 52 (2013) 439–448.

[56] B. Xu, D. Rathod, A. Yebi, Z. Filipi, S. Onori, M. Hoffman, A comprehensive review of organic rankine cycle waste heat recovery systems in heavy-duty diesel engine applications, Renew. Sustain. Energy Rev. 107 (2019) 145–170.

[57] E.H. Wang, H.G. Zhang, B.Y. Fan, M.G. Ouyang, Y. Zhao, Q.H. Mu, Study of working fluid selection of organic Rankine cycle (ORC) for engine waste heat recovery, Energy 36 (2011) 3406–3418.

[58] J.J. Bao, L. Zhao, A review of working fluid and expander selections for organic Rankine cycle, Renew. Sustain. Energy Rev. 24 (2013) 325–342.

[59] J. Kennedy, "Particle swarm optimization," in Encyclopedia of machine learning, ed: Springer, 2011, pp. 760-766.

[60] R.B. Atitallah, S. Niar, S. Meftali, J.-L. Dekeyser, An MPSoC performance estimation framework using transaction level modeling, *13th* IEEE International Conference on Embedded and Real-Time Computing Systems and Applications (RTCSA 2007), 2007, pp. 525–533.

[61] F. Leite, A. Akcamete, B. Akinci, G. Atasoy, S. Kiziltas, Analysis of modeling effort and impact of different levels of detail in building information models, Autom. Constr. 20 (2011) 601–609.

[62] F.B. Yang, X.R. Dong, H.G. Zhang, Z. Wang, K. Yang, J. Zhang, et al., Performance analysis of waste heat recovery with a dual loop organic Rankine cycle (ORC) system for diesel engine under various operating conditions, Energy Convers. Manage. 80 (2014) 243–255.

[63] S. Amicabile, J.I. Lee, D. Kum, A comprehensive design methodology of organic Rankine cycles for the waste heat recovery of automotive heavy-duty diesel engines, Appl. Therm. Eng. 87 (2015) 574–585.

[64] A. Hernandez, A. Desideri, C. Ionescu, S. Quoilin, V. Lemort, R. De Keyser, Increasing the efficiency of organic Rankine cycle technology by means of multivariable predictive control, Ifac Papersonline 47 (2014) 2195–2200.

[65] B. Xu, A. Yebi, D. Rathod, Z. Filipi, Real-time realization of dynamic programming using machine learning methods for IC engine waste heat recovery system power optimization, Appl. Energy (2019).